

## Key Points:

- The 1 in 10 year flux at  $L^* = 6.0$  ranges from  $4.35 \times 10^6 \text{ cm}^{-2} \text{ s}^{-1} \text{ sr}^{-1} \text{ MeV}^{-1}$  at  $E = 0.69 \text{ MeV}$  to  $1.16 \times 10^5 \text{ cm}^{-2} \text{ s}^{-1} \text{ sr}^{-1} \text{ MeV}^{-1}$  at  $E = 2.05 \text{ MeV}$
- The ratio of the 1 in 10 year flux at  $L^* = 6.0$  to that at  $L^* = 4.0$  ranges from 3.1 at  $E = 0.69 \text{ MeV}$  to 4.6 at  $E = 2.05 \text{ MeV}$
- The 1 in  $N$  year electron fluxes as a function of energy and  $L^*$  can serve as benchmarks against which to compare other extreme events

## Correspondence to:

N. P. Meredith,  
nmered@bas.ac.uk

## Citation:

Meredith, N. P., R. B. Horne, I. Sandberg, C. Papadimitriou, and H. D. R. Evans (2017), Extreme relativistic electron fluxes in the Earth's outer radiation belt: Analysis of INTEGRAL IREM data, *Space Weather*, 15, 917–933, doi:10.1002/2017SW001651.

Received 18 APR 2017

Accepted 30 JUN 2017

Accepted article online 7 JUL 2017

Published online 27 JUL 2017

©2017. The Authors.

This is an open access article under the terms of the Creative Commons Attribution License, which permits use, distribution and reproduction in any medium, provided the original work is properly cited.

## Extreme relativistic electron fluxes in the Earth's outer radiation belt: Analysis of INTEGRAL IREM data

Nigel P. Meredith<sup>1</sup> , Richard B. Horne<sup>1</sup> , Ingmar Sandberg<sup>2,3</sup>, Constantinos Papadimitriou<sup>2</sup>, and Hugh D. R. Evans<sup>4</sup> 

<sup>1</sup>British Antarctic Survey, Natural Environment Research Council, Cambridge, UK, <sup>2</sup>Space Applications and Research Consultancy, Athens, Greece, <sup>3</sup>Institute of Accelerating Systems and Applications, Athens, Greece, <sup>4</sup>European Space Research and Technology Centre, European Space Agency, Noordwijk, Netherlands

**Abstract** Relativistic electrons ( $E > 500 \text{ keV}$ ) cause internal charging and are an important space weather hazard. To assess the vulnerability of the satellite fleet to these so-called “killer” electrons, it is essential to estimate reasonable worst cases, and, in particular, to estimate the flux levels that may be reached once in 10 and once in 100 years. In this study we perform an extreme value analysis of the relativistic electron fluxes in the Earth's outer radiation belt as a function of energy and  $L^*$ . We use data from the Radiation Environment Monitor (IREM) on board the International Gamma Ray Astrophysical Laboratory (INTEGRAL) spacecraft from 17 October 2002 to 31 December 2016. The 1 in 10 year flux at  $L^* = 4.5$ , representative of equatorial medium Earth orbit, decreases with increasing energy ranging from  $1.36 \times 10^7 \text{ cm}^{-2} \text{ s}^{-1} \text{ sr}^{-1} \text{ MeV}^{-1}$  at  $E = 0.69 \text{ MeV}$  to  $5.34 \times 10^5 \text{ cm}^{-2} \text{ s}^{-1} \text{ sr}^{-1} \text{ MeV}^{-1}$  at  $E = 2.05 \text{ MeV}$ . The 1 in 100 year flux at  $L^* = 4.5$  is generally a factor of 1.1 to 1.2 larger than the corresponding 1 in 10 year flux. The 1 in 10 year flux at  $L^* = 6.0$ , representative of geosynchronous orbit, decreases with increasing energy ranging from  $4.35 \times 10^6 \text{ cm}^{-2} \text{ s}^{-1} \text{ sr}^{-1} \text{ MeV}^{-1}$  at  $E = 0.69 \text{ MeV}$  to  $1.16 \times 10^5 \text{ cm}^{-2} \text{ s}^{-1} \text{ sr}^{-1} \text{ MeV}^{-1}$  at  $E = 2.05 \text{ MeV}$ . The 1 in 100 year flux at  $L^* = 6.0$  is generally a factor of 1.1 to 1.4 larger than the corresponding 1 in 10 year flux. The ratio of the 1 in 10 year flux at  $L^* = 4.5$  to that at  $L^* = 6.0$  increases with increasing energy ranging from 3.1 at  $E = 0.69 \text{ MeV}$  to 4.6 at  $E = 2.05 \text{ MeV}$ .

### 1. Introduction

The twin drivers of globalization and technological advance have created a developed and developing world that are increasingly dependent on satellite technology for communication, navigation, Earth observation, and defence. For example, in 2015, the total revenue generated by the satellite industry was U.S. \$208.3 billion, an increase of 3% on the previous year [*Satellite Industry Association*, 2016]. This growing infrastructure is increasingly vulnerable to the damaging effects of space weather [*Krausmann*, 2011]. The concern is such that governments around the world now regard extreme space weather as a potential emergency situation [*Strategic National Risk Assessment*, 2011; *Cabinet Office*, 2012]. Establishing benchmarks for such events, including the determination of the 1 in 100 year event, is a key strategic goal of the U.S. government [*National Science and Technology Council*, 2015].

There are currently 1468 operational satellites in Earth orbit of which 556 are in geosynchronous orbit, 758 in low Earth orbit, 106 in medium Earth orbit, and 48 in elliptical orbit (<https://satellites.findthedata.com>). Extreme space weather events have a real capacity to damage this infrastructure, as happened during a major storm in 2003 when 10% of the satellite fleet experienced anomalies and one satellite was a complete loss [*Webb and Allen*, 2004].

Relativistic electrons are one of the most important space weather hazards. These, so-called “killer” electrons, can penetrate satellite surface materials and embed themselves in insulators and ungrounded conductors. This trapped charge can increase over time resulting in the build up of high electric fields that may eventually exceed that for breakdown leading to an internal electrostatic discharge [*Frederickson et al.*, 1991; *Rodgers and Ryden*, 2001]. The subsequent electric discharge can cause spurious signals, damage components, and, in extreme cases, lead to the complete loss of a satellite [e.g., *Koons and Fennell*, 2006]. Indeed, several studies have confirmed the link between satellite anomalies and the flux of relativistic electrons [*Wrenn*, 1995; *Wrenn et al.*, 2002; *lucci et al.*, 2005].

“Killer” electrons are found in two regions of near-Earth space, referred to as the inner and outer radiation belts. The inner radiation belt, which typically occurs at altitudes between 650 and 6500 km in the magnetic equatorial plane, is relatively stable. In sharp contrast, the outer radiation belt, which typically occurs at altitudes between 13,000 and 40,000 km, is highly dynamic with fluxes varying by several orders of magnitude on time scales ranging from minutes to weeks [e.g., *Blake et al.*, 1992; *Baker et al.*, 1994].

Global Navigation Satellite Systems (GNSS), which operate in medium Earth orbit and pass through the heart of the outer radiation belt, are exposed to large fluxes of relativistic electrons. Further out, communications satellites at geosynchronous orbit are located toward the edge of the outer radiation belt and may also be exposed to potentially damaging levels of relativistic electrons. Satellites in high inclination low Earth orbit are exposed to outer radiation belt electrons whenever they are located on geomagnetic field lines that map to this region and also to inner radiation belt electrons when they traverse the South Atlantic Anomaly.

The life expectancy of modern satellites in medium Earth orbit and at geosynchronous orbit is typically 10 to 20 years. Satellite operators, engineers, and insurers thus require estimates of the largest fluxes of relativistic electrons likely to be encountered on these and longer time scales. In particular, they require estimates of the 1 in 10, 1 in 50, and 1 in 100 year space weather event to try and determine how hostile the radiation environment could become in a worst case scenario. This information can be used to assess the likely impact of an extreme event on the satellite fleet and to improve the resilience of future satellites by better design of satellite components. Furthermore, published information on the likely magnitude of extreme events is very useful for satellite insurers in their dialogues with clients to assess if the latter are doing all they can to reduce risk. The information can also be used by the satellite insurers to evaluate realistic disaster scenarios, and to potentially reassess the reserves to be set aside to pay claims in the event of the occurrence of a worst case event.

Recent developments in the ways satellites are launched into geosynchronous orbit have implications for satellite instrumentation bound for this location. Traditionally, geosynchronous satellites are first launched into a geostationary transfer orbit and then a chemical propellant is used to raise the perigee to geosynchronous orbit. Satellites launched in this way typically take a few days traversing the heart of the Earth’s outer radiation belt on their way to their final orbit. However, the development of new technologies means that considerable savings can be made using electric orbit raising. After a traditional launch into a geosynchronous transfer orbit, the satellite undergoes gradual orbit raising using electric propulsion that may take 200 days or more to reach geosynchronous orbit. During this time the satellite may be exposed to higher levels of radiation than would be encountered at geosynchronous orbit. Indeed, a recent study has estimated that the radiation dose encountered by a satellite undergoing electric orbit raising for 200 days is equivalent to approximately 6.7 year operation at geostationary orbit or approximately half the typical design life [*Horne and Pitchford*, 2015]. A better understanding of worst case scenarios at different positions in the Earth’s outer radiation belt is valuable for both the satellite industry and satellite insurers as they endeavor to evaluate the potential vulnerabilities of this new technique to extreme space weather conditions.

In this study we used 14 years of data from the European Space Agency (ESA) International Gamma Ray Astrophysical Laboratory (INTEGRAL) satellite to determine the 1 in 10, 1 in 50, and 1 in 100 year space weather event for relativistic electrons in the outer radiation belt as a function of energy and  $L^*$ . We determined the number of times the fluxes rose above selected thresholds and computed probability distributions at  $L^* = 4.5$  and 6.0. We then conducted extreme value analyses to determine the 1 in 10, 1 in 50, and 1 in 100 year flux as a function of energy and  $L^*$ . The instrumentation and data analysis are described in section 2, and the probability distributions are presented in section 3. The extreme value analysis technique is briefly described in section 4, and the results are presented in section 5. Finally, the results are discussed and the conclusions presented in sections 6 and 7, respectively.

## 2. Instrumentation and Data Analysis

### 2.1. Instrumentation

The data used in this study were collected by the Radiation Environment Monitor (IREM) on board ESA’s INTEGRAL satellite. This instrument is a modified version of ESA’s Standard Radiation Environment Monitor (SREM), a space-dedicated detector assembly designed to measure high-energy electrons and protons [*Mohammadzadeh et al.*, 2003]. The unit also provides the host spacecraft with radiation information, enabling other instruments to be autonomously switched into a safe mode in the event of high radiation levels.

The INTEGRAL satellite was launched on 17 October 2002 into a highly elliptical, high inclination orbit (52.25°) with a perigee altitude of 9000 km, an apogee altitude of 153,000 km and an orbital period of three sidereal days. The original mission lifetime was 2.5 years with a possible extension of another 2.5 years. However, due to the high scientific return and good performance of the instruments, the mission has been regularly extended and, after 14 years, continues to acquire good quality scientific data.

The IREM unit on board INTEGRAL consists of three silicon diode detectors (D1, D2, and D3) in a two-detectors-head configuration. One system consists of two silicon diode detectors (D1/D2) one after the other, in a coaxial configuration (detector telescope configuration) and the other system is a single silicon diode detector (D3) as depicted, schematically, in Figure 2 of Siegl *et al.* [2010]. The D1/D2 and D3 detector entrances have opening angles of  $\pm 20^\circ$ . For the coincidence counters the acceptance angle is essentially restricted by the aperture. However, ultra high energy particles may penetrate from any direction [Siegl *et al.*, 2010].

The main entrance of the D1/D2 detector configuration is covered with a 2 mm aluminum layer which sets a low-energy cutoff of  $\sim 1.5$  and  $\sim 20$  MeV for electrons and protons respectively. The D3 detector is covered with a 0.7 mm aluminum layer, setting its thresholds for electrons and protons at  $\sim 0.5$  MeV and  $\sim 10$  MeV, respectively. The diodes of the telescope configuration are separated by a 1.7 mm thick aluminum and a 0.7 mm thick tantalum layer. In addition, the shielding between the two diodes in the telescope prevents the passage of electrons. Thus, using the two diodes in coincidence gives pure proton count rates. However, in the presence of ultrarelativistic electrons ( $E > 8$  MeV), the C4 coincidence channel can be contaminated by electron counts [Evans *et al.*, 2008]. All preamplified detector pulses are scrutinized by a set of 15 fast comparators (channels)—11 for single events and 4 for coincidences—providing energy spectral information. IREM samples the spectra in broad and overlapping energy bands, so that the count rates of the channels are strongly dependent on each other.

In this study we focus on the largest count rates observed by IREM, and it is important to correct them for the effects of dead time. The dead time of each of the three detectors is directly measured by the use of three additional dead time counters  $PL_{i=1,2,3}$ . When an event is detected by a given detector the electronics opens a gate which is subsequently closed when the output signal goes below the lowest threshold of that detector. No new event is accepted while the gate remains open. For each accumulation period, the instrument counts the number of times,  $N_{PL_i}$ , that each gate is open at a default sampling rate,  $N_{check}$ , of 1 kHz. These measurements are then used to correct the counts measured by each detector,  $C_{di}$  for the effects of dead time. The corrected count rate for each detector,  $C_{di,corr}$  is then given by

$$C_{di,corr} = C_{di} \left( 1 - \frac{N_{PL_i}}{N_{check} t_{acc}} \right)^{-1} \quad (1)$$

where  $t_{acc} = 60$  s is the accumulation time. The dead time correction depends considerably on the detector and the integration time. For example, the D3 detector dead time correction during the April 2010 event peaked at  $\sim 1.6$ . This was for a particularly high count rate. Further details of the IREM instrument are given in Evans *et al.* [2008].

### 2.1.1. Conversion of IREM Count Rates to Fluxes

The count rates provided by the 15 channels,  $C_i$ ,  $i = 1..15$ :

$$C_i = \sum_{q=p,e} \int_0^\infty f_q(E) RF_{i,q}(E) dE, \quad (2)$$

are given by the convolution of the incident proton and electron (omnidirectional) differential fluxes  $f_q(E)$  ( $\text{cm}^{-2} \text{s}^{-1} \text{MeV}^{-1}$ ) and the corresponding response functions  $RF_{i,q}(E)$ , where the sum over  $q$  is performed for protons, p and electrons, e. The calculation of  $f_q(E)$  requires the inversion of equation (2). This requires careful analysis, since the solution  $f_q(E)$  is not unique. For the calculation of IREM fluxes we applied the scheme developed by Sandberg *et al.* [2012]. The scheme applies iteratively the regularized singular value decomposition (SVD) method [Höcker and Kartvelishvili, 1996] over different electron (or proton) energy ranges and leads to the derivation of multiple numerical solutions for the electron (proton) flux spectra. The final solution is constructed by choosing the maximum flux value over the derived solutions for each energy bin as detailed in Sandberg *et al.* [2012].

The applied technique and the resulting IREM proton and electron fluxes have been evaluated using updated reference data sets. For the proton fluxes the second version (2.0) of the ESA Solar Energetic Particle

**Table 1.** Electron Energies and Derived Correction Factors

Energy (MeV)	Correction Factor
0.69	2.85
0.78	2.05
0.88	1.77
0.99	1.64
1.12	1.47
1.27	1.19
1.43	0.96
1.61	0.79
1.82	0.63
2.05	0.58

Environment Modeling (SEPEM) Reference Data Set (RDS) was used. SEPEM RDS 2.0 is a data set resulting from the merging of cross-calibrated measurements from the Energetic Particle Sensors on board the GOES satellites with the high-energy resolution Goddard Medium Energy Experiment (GME) on IMP-8 [Sandberg *et al.*, 2014]. For the electron fluxes, a large number (~400) of suitable magnetic conjunctions between IREM on board INTEGRAL and the Magnetic Electron Ion Spectrometer (MagEIS) instruments [Blake *et al.*, 2013] on board the Van Allen probe B were found and analyzed. As a result of this analysis, scaling

factors for the IREM SVD electron fluxes were determined. The scaling factors were defined as the factors  $sf(E)$  that minimize  $RMS(E) = (\sum_t (f_{e, MagEIS}(E, t) - f_{e, IREM}(E, t) * sf(E))^2)^{1/2}$ . These factors were found to decrease with energy and range from 2.85 (for 0.69 MeV) to 0.58 (for 2.05 MeV) (cf. Table 1).

## 2.2. Data Analysis

The perigee and apogee altitudes and inclination of the INTEGRAL orbit vary considerably throughout the mission, primarily due to the Earth's oblateness and luni-solar gravitational perturbations. During any given orbit the Earth's radiation belts are typically crossed at both high and low magnetic latitudes [e.g., Hübner *et al.*, 2012]. Flat-topped pitch angle distributions are characteristic of relativistic electron enhancements [Horne *et al.*, 2003]. These pitch angle distributions have broad flat tops and typically fall off at smaller pitch angles (<50°). Therefore, to reduce the effect of changing flux at smaller pitch angles we select data from within 15° of the magnetic equator.

The orbital period of three sidereal days (71.803 h) was maintained actively from launch until early 2015 when ESA performed a series of manoeuvres toward a safe disposal in February 2029, via natural reentry into the atmosphere. These operations took place from 13 January to 12 February 2015. The resulting orbit has a repeating pattern of three revolutions in eight sidereal days, resulting in an orbital period of 63.825 h. The extreme value analysis requires that the data are equally spaced in time and so, after 13 January 2015, for any given  $L^*$  we use the maximum value recorded in any 71.803 h window. In this way we capture the largest values recorded while at the same time maintaining an equal time step between the data points. Note that since the extreme value analysis technique includes a declustering process to ensure that each relativistic enhancement is counted only once, if two data points occur in one 71.803 h window that are both above the threshold, no extreme values are lost from the resulting analysis, since, had we processed the data at the smaller time step, the smaller of the two extreme values would have been excluded by the declustering process (see section 4).

From the resulting database we determined the electron flux in the vicinity of the magnetic equator for 12 evenly spaced  $L^*$  values from  $L^* = 4.00$  to  $L^* = 6.75$ . For each  $L^*$  we calculated the average flux over a  $0.2L^*$  bin centered on the given  $L^*$ . The magnetic coordinate  $L^*$  was calculated using the UNILIB software library (<http://www.mag-unilib.eu/>), adopting the International Geomagnetic Reference Field in the middle of the appropriate year together with the Olson-Pfitzer quiet time model [Olson and Pfitzer, 1977].

Figure 1 shows the data coverage for selected  $L^*$ . From top to bottom the panels show the  $E = 1.27$  MeV electron flux at  $L^* = 6.5, 6.0, 5.5, 5.0, 4.5, 4.0$ , and the sunspot number as a function of time. The coverage is good, but not identical at all  $L^*$  values with the solar cycle being well covered. The coverage ranges from a minimum of 1042 data points at  $L^* = 4.0$  to a maximum of 1245 data points at  $L^* = 6.5$ , corresponding to a minimum and maximum data coverage of 8.5 and 10.2 years, respectively. We produced monthly and yearly summary plots in a similar format showing the data at each  $L^*$  value and energy and inspected them for outliers. The electron flux data were confirmed to be very clean and no outliers were found. To help assess the satellite environment, we also downloaded and stored the geomagnetic indices and solar wind parameters at a 1 h resolution.

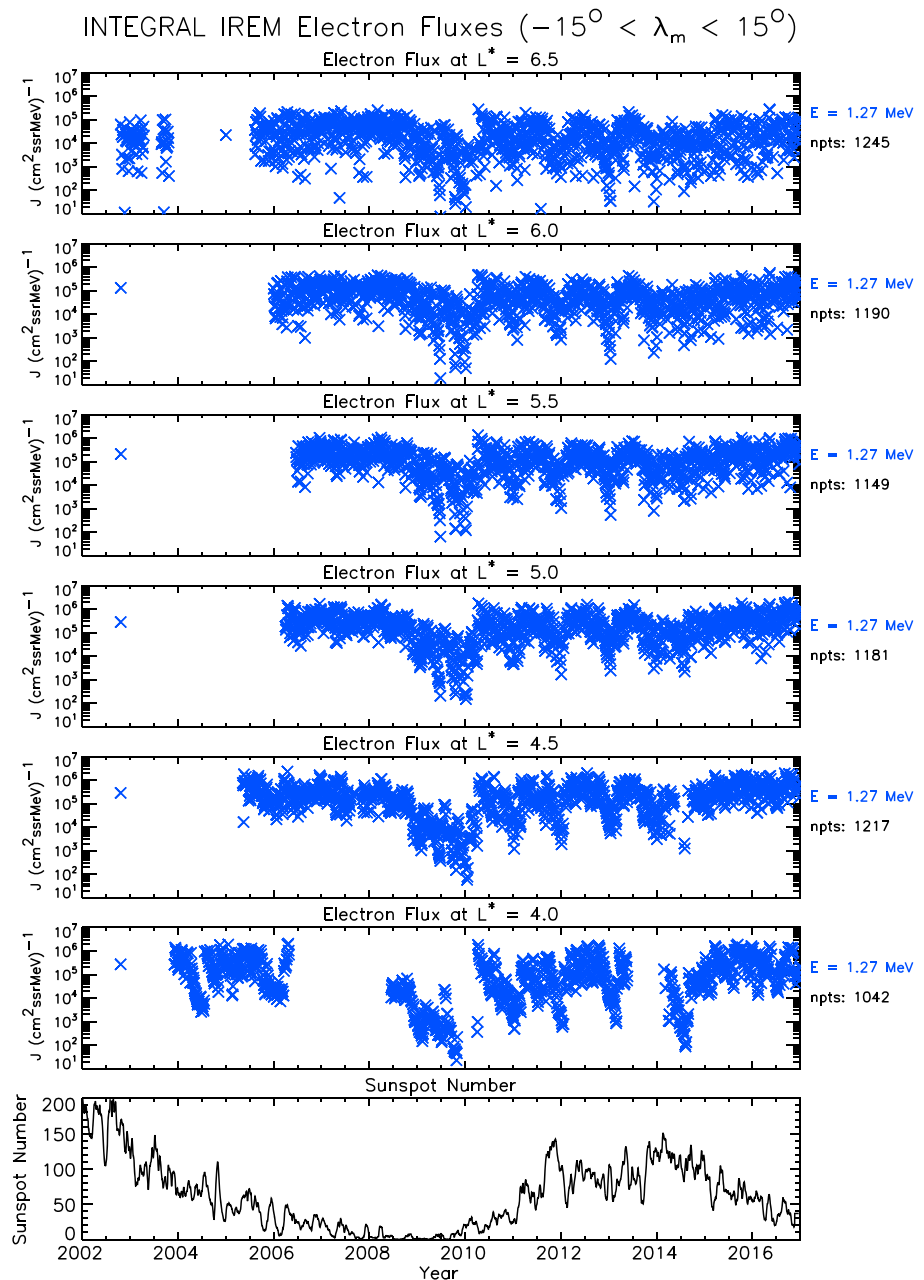


**Figure 1.** Plot of the  $E = 1.27$  MeV electron fluxes and the sunspot number as a function of time. From top to bottom the panels show the  $E = 1.27$  MeV electron flux at  $L^* = 6.5, 6.0, 5.5, 5.0, 4.5, 4.0$ , and the sunspot number.

### 3. Statistics

Figure 2 shows a summary plot for 2016 for two representative  $L^*$  values. We choose  $L^* = 4.5$  as representative of the location of the peak fluxes in GNSS type environments and  $L^* = 6.0$  as representative of the conditions at geosynchronous orbit. To put the data in context, the plots also show the GOES  $E > 2$  MeV electron flux at geosynchronous orbit [Onsager et al., 1996], together with relevant solar wind parameters and geophysical indices. From top to bottom the panels show the GOES  $E > 2$  MeV electron flux at a 5 min time resolution, the IREM electron fluxes for selected electron energies at  $L^* = 6.0$  and  $4.5$ , the solar wind speed and the  $IMFBz$  in GSM coordinates, the  $Dst$  index and solar wind pressure, and the  $Kp$  (color coded) and  $AE$  indices. In the panels showing the IREM electron fluxes, the symbols are color coded according to electron energy. The symbols

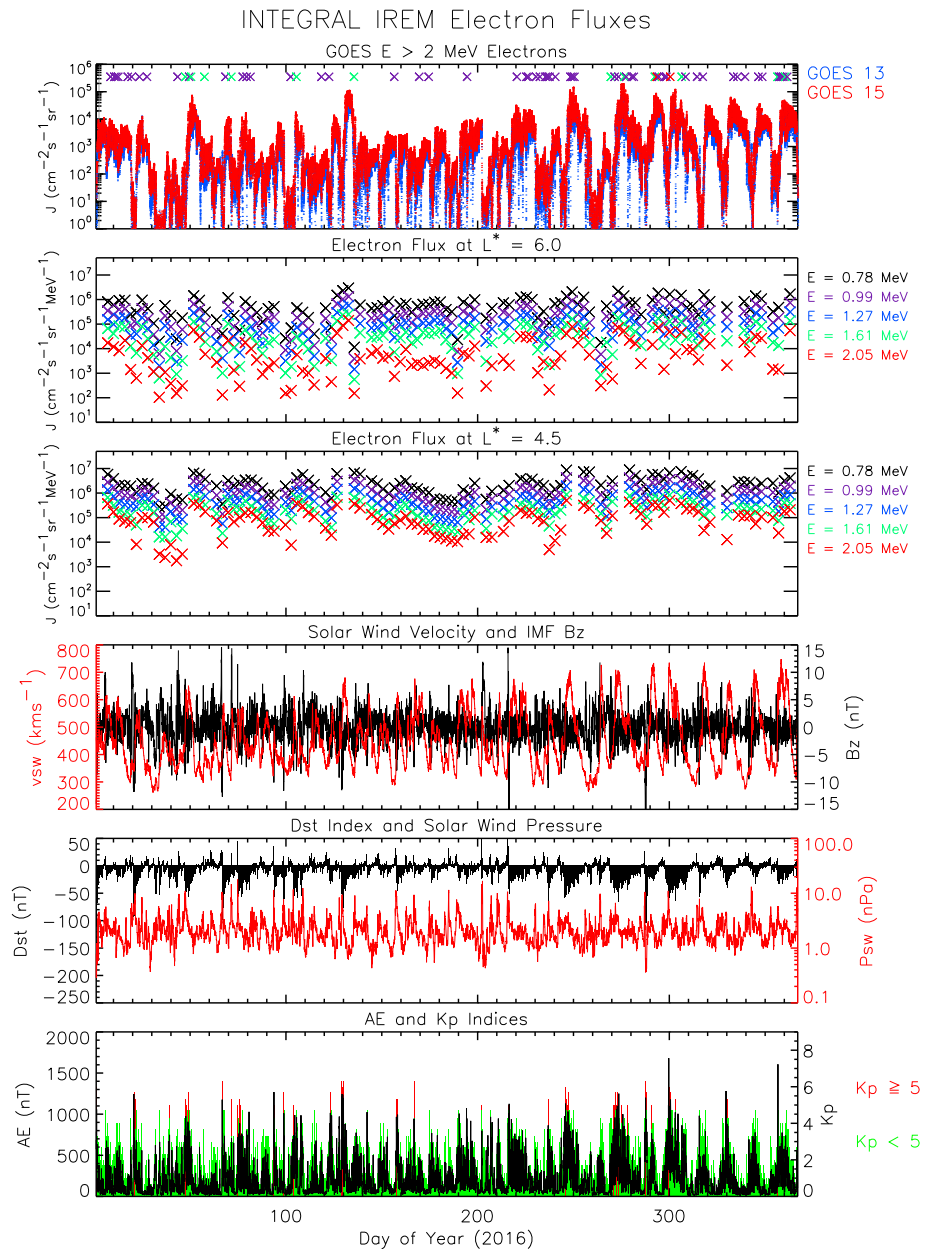


**Figure 2.** Summary plot of the IREM fluxes from 2016. From top to bottom, the panels show the GOES  $E > 2$  MeV electron flux, the IREM electron flux, the IREM electron fluxes for  $L^* = 6.0$  and  $4.5$ , the solar wind speed and the  $IMFBz$  in GSM coordinates, the  $Dst$  index and solar wind pressure, and the  $Kp$  (color coded) and  $AE$  indices. In Figure 2 (first panel) the symbols represent days with one (purple), two (green), or three (red) anomalies attributed to IESD as determined from 37 satellites in geosynchronous orbit. In the panels showing the IREM fluxes, the colored symbols represent selected electron energies as listed to the right of the panels.

in Figure 2 (first panel) represent days with anomalies attributed to internal electrostatic discharges (IESD), determined from 37 operational satellites in geosynchronous orbit (D. Pitchford, personal communication, 2017). Days with one, two, and three anomalies attributed to IESD are coded purple, green, and red, respectively.

This period is characterized by a number of significant flux increases caused by recurrent high-speed solar wind streams. Indeed, some of the largest fluxes in the history of the mission were observed during the year. For example, on 26 October 2016 the flux of  $E = 2.05$  MeV electrons reached  $5.04 \times 10^5 \text{ cm}^{-2} \text{ s}^{-1} \text{ sr}^{-1} \text{ MeV}^{-1}$  at  $L^* = 4.5$  and was the third largest event at this location and energy. Further out, at  $L^* = 6.0$ , the flux

**Table 2.** Largest Electron Fluxes Observed at  $E = 0.69, 1.27, \text{ and } 2.05 \text{ MeV}$  at  $L^* = 4.5$

0.69 MeV		1.27 MeV		2.05 MeV	
Flux ( $\text{cm}^2 \text{ s sr MeV}^{-1}$ )	Date	Flux ( $\text{cm}^2 \text{ s sr MeV}^{-1}$ )	Date	Flux ( $\text{cm}^2 \text{ s sr MeV}^{-1}$ )	Date
$1.42 \times 10^7$	15 Apr 2006	$2.30 \times 10^6$	15 Apr 2006	$5.65 \times 10^5$	15 Apr 2006
$1.36 \times 10^7$	5 Oct 2016	$1.96 \times 10^6$	17 Jul 2012	$5.10 \times 10^5$	17 Jul 2012
$1.35 \times 10^7$	2 Sep 2016	$1.92 \times 10^6$	2 Sep 2016	$5.04 \times 10^5$	26 Oct 2016
$1.18 \times 10^7$	1 Nov 2016	$1.82 \times 10^6$	5 Oct 2016	$5.03 \times 10^5$	2 Sep 2016
$1.17 \times 10^7$	17 Jul 2012	$1.74 \times 10^6$	18 May 2005	$4.96 \times 10^5$	18 May 2005
$1.14 \times 10^7$	11 Sep 2016	$1.72 \times 10^6$	14 Nov 2015	$4.26 \times 10^5$	14 Nov 2015
$1.14 \times 10^7$	14 Nov 2015	$1.67 \times 10^6$	26 Oct 2016	$4.25 \times 10^5$	5 Oct 2016
$1.13 \times 10^7$	14 Sep 2016	$1.59 \times 10^6$	16 Dec 2006	$4.25 \times 10^5$	13 Sep 2011
$1.11 \times 10^7$	18 May 2005	$1.58 \times 10^6$	1 Nov 2016	$4.24 \times 10^5$	2 Jun 2005
$1.08 \times 10^7$	27 May 2007	$1.54 \times 10^6$	22 Mar 2015	$4.18 \times 10^5$	5 Aug 2010

of  $E = 2.05 \text{ MeV}$  electrons reached  $1.40 \times 10^5 \text{ cm}^{-2} \text{ s}^{-1} \text{ sr}^{-1} \text{ MeV}^{-1}$  on 11 May 2016 and was the largest event at this location and energy.

The top 10 fluxes of  $E = 0.69, E = 1.27, \text{ and } E = 2.05 \text{ MeV}$  electrons at  $L^* = 4.5$  and  $L^* = 6.0$  are tabulated in Tables 2 and 3, respectively. The largest electron fluxes observed at  $L^* = 4.5$ , occurred on 15 April 2006 and were  $1.42 \times 10^7 \text{ cm}^{-2} \text{ s}^{-1} \text{ sr}^{-1} \text{ MeV}^{-1}$ ,  $2.30 \times 10^6 \text{ cm}^{-2} \text{ s}^{-1} \text{ sr}^{-1} \text{ MeV}^{-1}$ , and  $5.65 \times 10^5 \text{ cm}^{-2} \text{ s}^{-1} \text{ sr}^{-1} \text{ MeV}^{-1}$ , respectively. The largest fluxes at  $L^* = 6.0$  were factors of 3, 4, and 4 lower for each energy, respectively, and all occurred on 11 May 2016.

We then determined the number of times the fluxes of the  $E = 0.69, E = 1.27, \text{ and } E = 2.05 \text{ MeV}$  electrons exceeded selected thresholds as a function of  $L^*$ . The results are presented in Table 4. The largest fluxes were typically seen in the region  $4.0 \leq L^* \leq 5.0$ . For example, the  $E = 0.69 \text{ MeV}$  electron flux exceeded  $5.0 \times 10^6 \text{ cm}^{-2} \text{ s}^{-1} \text{ sr}^{-1} \text{ MeV}^{-1}$  for over 10% of the measurements in this region. At  $E = 2.05 \text{ MeV}$  the electron flux exceeded  $2.0 \times 10^5 \text{ cm}^{-2} \text{ s}^{-1} \text{ sr}^{-1} \text{ MeV}^{-1}$  for over 8% of the measurements in the region  $4.0 \leq L^* \leq 4.75$ .

The distributions of the electron fluxes at  $L^* = 4.5$  are shown in Figure 3a. The observed fluxes at any given energy cover over 3 orders of magnitude. The largest observed fluxes cover over an order of magnitude, ranging from  $1.42 \times 10^7 \text{ cm}^{-2} \text{ s}^{-1} \text{ sr}^{-1} \text{ MeV}^{-1}$  at  $E = 0.69 \text{ MeV}$  to  $5.65 \times 10^5 \text{ cm}^{-2} \text{ s}^{-1} \text{ sr}^{-1} \text{ MeV}^{-1}$  at  $E = 2.05 \text{ MeV}$ . The fluxes corresponding to selected exceedance probabilities are shown as a function of energy in Figure 3c. The 0.1% exceedance level decreases with energy ranging from  $1.41 \times 10^7 \text{ cm}^{-2} \text{ s}^{-1} \text{ sr}^{-1} \text{ MeV}^{-1}$  at  $E = 0.69 \text{ MeV}$  to  $5.53 \times 10^5 \text{ cm}^{-2} \text{ s}^{-1} \text{ sr}^{-1} \text{ MeV}^{-1}$  at  $E = 2.05 \text{ MeV}$ .

**Table 3.** Largest Electron Fluxes Observed at  $E = 0.69, 1.27, \text{ and } 2.05 \text{ MeV}$  at  $L^* = 6.0$

0.69 MeV		1.27 MeV		2.05 MeV	
Flux ( $\text{cm}^2 \text{ s sr MeV}^{-1}$ )	Date	Flux ( $\text{cm}^2 \text{ s sr MeV}^{-1}$ )	Date	Flux ( $\text{cm}^2 \text{ s sr MeV}^{-1}$ )	Date
$4.60 \times 10^6$	11 May 2016	$5.74 \times 10^5$	11 May 2016	$1.40 \times 10^5$	11 May 2016
$4.26 \times 10^6$	11 Apr 2010	$4.87 \times 10^5$	8 May 2016	$1.02 \times 10^5$	11 Apr 2010
$3.94 \times 10^6$	8 Apr 2010	$4.74 \times 10^5$	11 Apr 2010	$9.78 \times 10^4$	30 Mar 2008
$3.88 \times 10^6$	30 May 2013	$4.64 \times 10^5$	5 May 2010	$9.73 \times 10^4$	8 Apr 2010
$3.79 \times 10^6$	30 May 2007	$4.51 \times 10^5$	3 Mar 2008	$9.67 \times 10^4$	9 Oct 2015
$3.72 \times 10^6$	16 Dec 2006	$4.50 \times 10^5$	8 Apr 2010	$8.99 \times 10^4$	30 May 2007
$3.71 \times 10^6$	3 Mar 2008	$4.31 \times 10^5$	30 May 2013	$8.84 \times 10^4$	8 May 2016
$3.64 \times 10^6$	5 May 2010	$4.29 \times 10^5$	30 Mar 2008	$8.66 \times 10^4$	6 Apr 2007
$3.57 \times 10^6$	8 May 2016	$4.26 \times 10^5$	30 Apr 2007	$8.36 \times 10^4$	2 Apr 2008
$3.48 \times 10^6$	2 Apr 2008	$4.24 \times 10^5$	9 Oct 2015	$8.25 \times 10^4$	3 Mar 2008

**Table 4.** Percentage of Times the Flux Exceeds Certain Thresholds

$L^*$	$n$	0.69 MeV			1.27 MeV			2.05 MeV		
		$10^6$	$2 \times 10^6$	$5 \times 10^6$	$2 \times 10^5$	$5 \times 10^5$	$10^6$	$5 \times 10^4$	$10^5$	$2 \times 10^5$
4.00	1042	44	30	11	33	16	5.5	27	16	8.6
4.25	1092	54	35	13	38	19	7.1	31	19	9.2
4.50	1217	62	41	13	46	20	6.7	34	20	9.3
4.75	1195	64	42	13	49	19	5.6	34	18	8.7
5.00	1181	65	41	11	47	18	4.3	33	17	4.6
5.25	1167	62	35	6.4	42	14	1.7	24	11	3.9
5.50	1149	54	25	3.1	33	6.5	0.3	16	6.4	1.1
5.75	1160	42	16	1.0	22	2.2	0	8.5	2.8	0
6.00	1190	27	6.8	0	11	0	0	3.2	0.1	0
6.25	1188	18	1.9	0	3.5	0	0	0.5	0	0
6.50	1245	6.9	0.2	0	0.5	0	0	0.1	0	0
6.75	1162	1.7	0	0	0	0	0	0	0	0

Statistical Analysis of INTEGRAL IREM Electron Fluxes  
Exceedance Probability

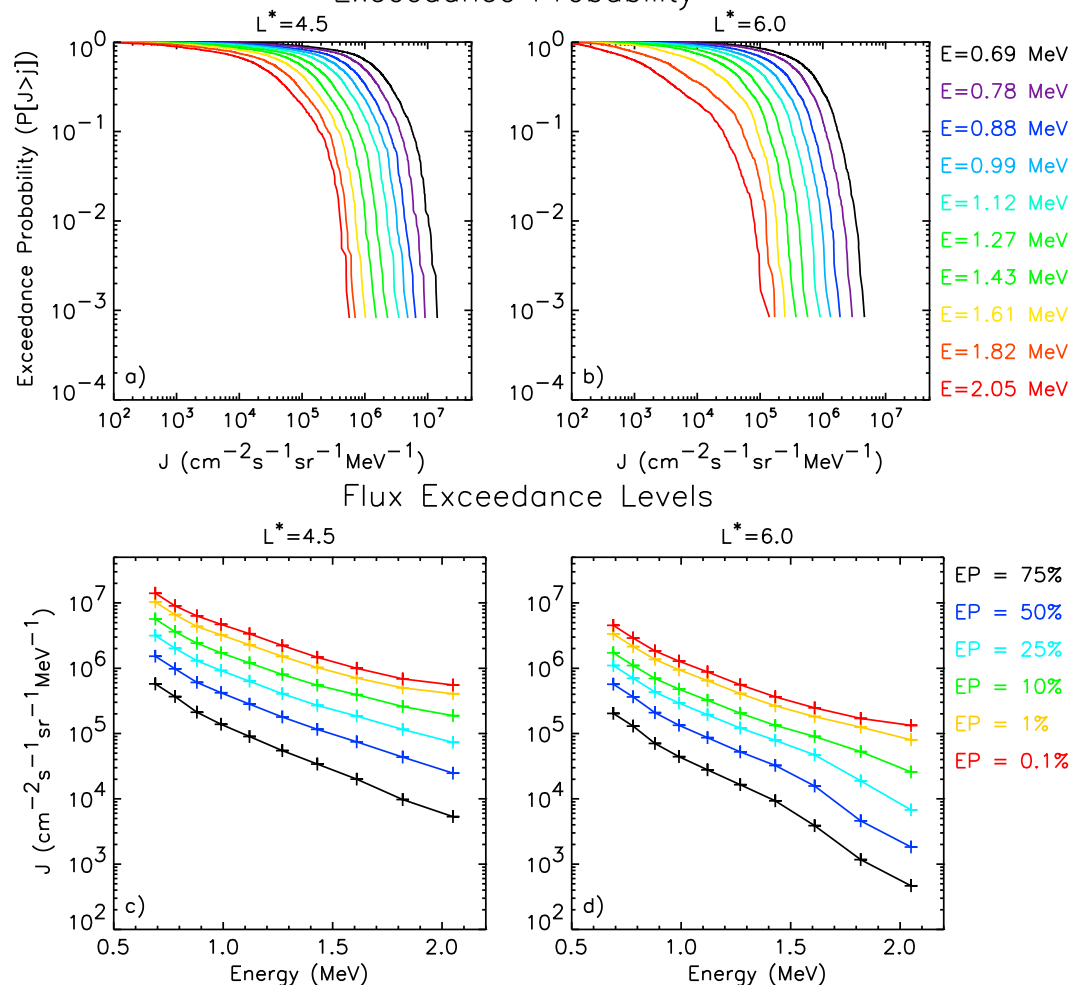


**Figure 3.** Plots of the exceedance probabilities for (a)  $L^* = 4.5$  and (b)  $L^* = 6.0$  for each electron energy and flux exceedance levels as a function of energy at (c)  $L^* = 4.5$  and (d)  $L^* = 6.0$ .

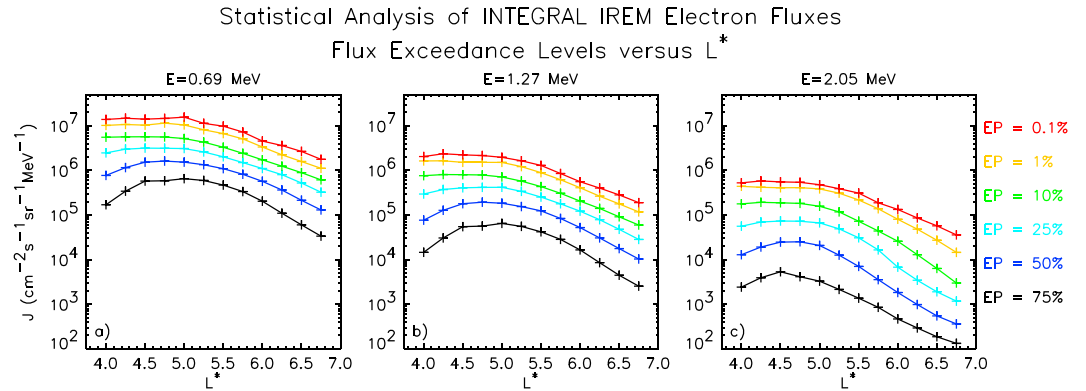


**Figure 4.** Plots of the flux exceedance levels as a function of  $L^*$  for (a)  $E = 0.69$  MeV electrons, (b)  $E = 1.27$  MeV electrons and (c)  $E = 2.05$  MeV electrons.

The distributions of the electron fluxes at  $L^* = 6.0$  are shown in Figure 3b. The observed fluxes at any given energy cover over 3 orders of magnitude. The largest observed fluxes again cover over an order of magnitude, ranging from  $4.60 \times 10^6 \text{ cm}^{-2} \text{ s}^{-1} \text{ sr}^{-1} \text{ MeV}^{-1}$  at  $E = 0.69$  MeV to  $1.40 \times 10^5 \text{ cm}^{-2} \text{ s}^{-1} \text{ sr}^{-1} \text{ MeV}^{-1}$  at  $E = 2.05$  MeV. The fluxes corresponding to selected exceedance probabilities are shown as a function of energy in Figure 3d. The 0.1% exceedance level decreases with energy ranging from  $4.53 \times 10^6 \text{ cm}^{-2} \text{ s}^{-1} \text{ sr}^{-1} \text{ MeV}^{-1}$  at  $E = 0.69$  MeV to  $1.33 \times 10^5 \text{ cm}^{-2} \text{ s}^{-1} \text{ sr}^{-1} \text{ MeV}^{-1}$  at  $E = 2.05$  MeV.

The fluxes for selected exceedance levels are shown as a function of  $L^*$  for three selected energies in Figure 4. The median flux of relativistic electrons peaks at  $L^* = 4.75$  for each energy. However, for exceedance levels above 10%, for any given energy, the fluxes are relatively constant in the region  $4.0 \leq L^* \leq 5.0$  and then decrease with increasing  $L^*$  in the region  $5.0 \leq L^* \leq 6.75$ .

#### 4. Extreme Value Analysis

We performed an extreme value analysis of the electron fluxes as a function of energy and  $L^*$  using the exceedances over the threshold method described in Meredith *et al.* [2015]. The threshold at each energy and  $L^*$  should be low enough to include a meaningful number of data points and high enough to capture the behavior of the tail of the distribution. Based on experience analyzing other satellite data sets [e.g., Meredith *et al.*, 2015, 2016a], for each energy and  $L^*$  we set the threshold at the 2% exceedance level. We declustered the data by assuming a cluster to be active until two consecutive measurements fell below the chosen threshold. We then fitted the generalized Pareto distribution (GPD) [Picklands, 1975; Coles, 2001] to the cluster maxima as a function of energy and  $L^*$  using the ismev library routine `gpd.fit` [Heffernan *et al.*, 2014] provided in the R statistical package [R Development Core Team, 2008]. The GPD may be written as

$$G(y) = 1 - \left(1 + \frac{\xi y}{\sigma}\right)^{-\frac{1}{\xi}} \quad (3)$$

where  $y = (x - u)$  are the exceedances,  $x$  are the cluster maxima above the chosen threshold,  $u$ ,  $\xi$  is the shape parameter, and  $\sigma$  the scale parameter [Coles, 2001]. The sign of the shape parameter provides important information on the behavior of the tail of the distribution. If  $\xi$  is positive, the distribution has no upper limit, whereas if  $\xi$  is negative, the distribution has an upper bound. The level,  $x_N$ , which is exceeded on average once every  $N$  years may be expressed in terms of  $\xi$  and  $\sigma$  as:

$$x_N = u + \frac{\sigma}{\xi} \left( (N n_d n_c / n_{\text{tot}})^{\xi} - 1 \right) \quad (4)$$

where  $n_c$  is the number of clusters,  $n_{\text{tot}}$  is the total number of data points, and  $n_d = 122$  is the number of measurements in any given year [Coles, 2001].

#### 5. Results

To demonstrate the method used, we first show the results for  $E = 1.27$  MeV electrons at  $L^* = 4.5$ . The  $E = 1.27$  MeV electron flux is shown as a function of time in Figure 5 (top). The 2% exceedance level of

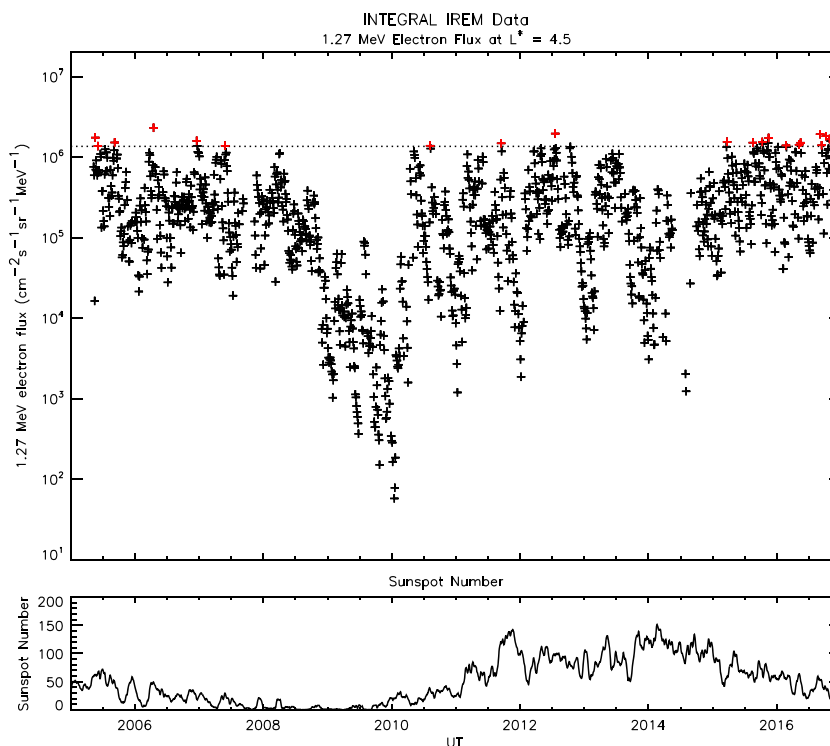


**Figure 5.** Plot of the  $E = 1.27$  MeV electron flux as a function of time at  $L^* = 4.5$ . (top) The 2% exceedance level, chosen as the threshold for the extreme value analysis, is shown as a dotted line and the cluster maxima are coded red. (bottom) Trace of the sunspot number as a function of UT time.

$1.36 \times 10^6 \text{ cm}^{-2} \text{ s}^{-1} \text{ sr}^{-1} \text{ MeV}^{-1}$  is shown as the dashed line, and the cluster maxima are coded red. Figure 5 (bottom) shows the sunspot number. The largest fluxes of  $E = 1.27$  MeV electrons at  $L^* = 4.5$  tend to be seen during the declining and ascending phases of the solar cycle with lower fluxes typically being seen around solar minimum and solar maximum.

The scale and shape parameters for the fit to the cluster maxima of  $E = 1.27$  MeV electrons at  $L^* = 4.5$  are determined to be  $(2.7 \pm 0.1) \times 10^5$  and  $-0.08 \pm 0.15$ , respectively. The shape parameter is marginally negative, but the error bar covers both positive and negative values. Thus, it is not possible to infer the presence or absence of a limiting flux from this observation alone. Figure 6a shows the probability plot for the cluster maxima of the  $E = 1.27$  MeV electron flux. The best fit straight line to the data points is shown in blue and has a correlation coefficient of 0.993. Figure 6b shows the quantile plot for the cluster maxima of the  $E = 1.27$  MeV electron flux. The best fit straight line is again shown in blue and has a correlation coefficient of 0.993. The fact that both fits are approximately linear suggests that the generalized Pareto model is a good method for modeling the exceedances [e.g., Coles, 2001].

Figure 6c shows the exceedance probability of the cluster maxima above the threshold value of  $1.36 \times 10^6 \text{ cm}^{-2} \text{ s}^{-1} \text{ sr}^{-1} \text{ MeV}^{-1}$ ,  $(P[J > j | J > u])$  (black symbols), together with the maximum likelihood fit (blue line). Figure 6d shows the flux that is exceeded on average once every  $N$  years as a function of  $N$  for the declustered  $E = 1.27$  MeV electron flux. The 1 in  $N$  year return level determined from equation (2) is shown as the solid blue line, and the symbols represent the experimental return levels. The 95% confidence interval of the 1 in  $N$  year return levels are shown as the dotted blue lines. The 1 in 10, 1 in 50, and 1 in 100 year  $E = 1.27$  MeV electron fluxes at  $L^* = 4.5$  are  $2.08 \times 10^6$ ,  $2.39 \times 10^6$  and  $2.52 \times 10^6 \text{ cm}^{-2} \text{ s}^{-1} \text{ sr}^{-1} \text{ MeV}^{-1}$ .

We repeated the analysis for each electron energy at  $L^* = 4.5$  and determined the corresponding 1 in  $N$  year events. The results for  $N = 10, 50$ , and 100 years are shown in Figure 7a. The 1 in 10 year flux (black line) decreases with increasing energy and ranges from  $1.36 \times 10^7 \text{ cm}^{-2} \text{ s}^{-1} \text{ sr}^{-1} \text{ MeV}^{-1}$  at  $E = 0.69$  MeV to  $5.34 \times 10^5 \text{ cm}^{-2} \text{ s}^{-1} \text{ sr}^{-1} \text{ MeV}^{-1}$  at 2.05 MeV. The 1 in 100 year event (red line) exhibits a similar trend, lying in the range  $1.46 \times 10^7 \text{ cm}^{-2} \text{ s}^{-1} \text{ sr}^{-1} \text{ MeV}^{-1}$  to  $5.79 \times 10^5 \text{ cm}^{-2} \text{ s}^{-1} \text{ sr}^{-1} \text{ MeV}^{-1}$  and is a factor of 1.1 to 1.2 larger than the corresponding 1 in 10 year event. Figure 7c shows the shape parameter for the electron flux

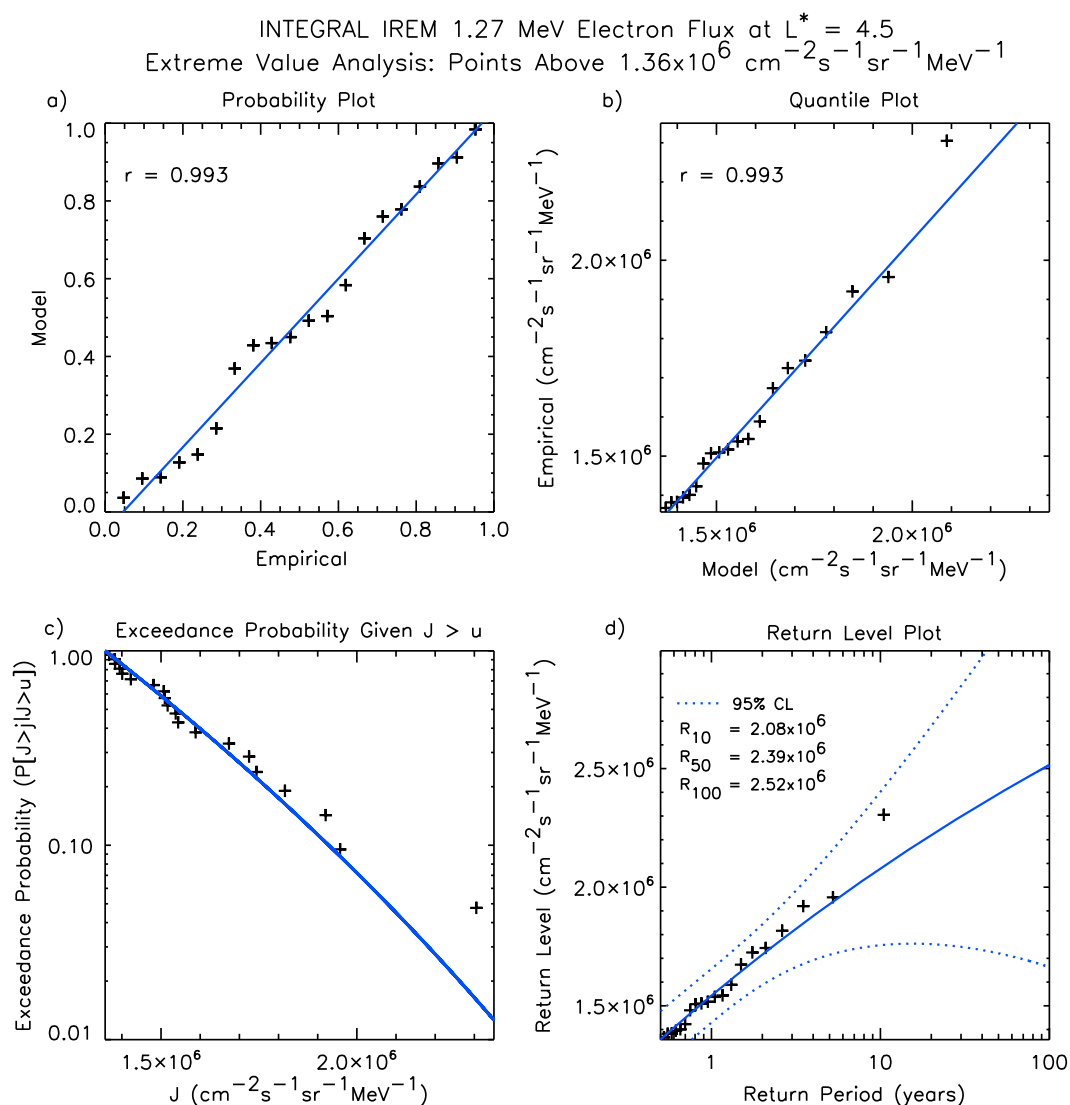


**Figure 6.** Extreme value analysis for the flux of  $E = 1.27$  MeV electrons at  $L^* = 4.5$ . (a) Probability plot, (b) quantile plot, (c) the exceedance probability given  $J > u$ , and (d) the return level plot.

at  $L^* = 4.5$  as a function of energy. The shape parameter is predominantly negative at each energy, suggesting the relativistic electron fluxes at  $L^* = 4.5$  have energy-dependent upper limits.

We then repeated the analysis for each electron energy at  $L^* = 6.0$ . The results for  $N = 10, 50$ , and 100 years are shown in Figure 7b. The 1 in 10 year flux (black line) decreases with increasing energy and ranges from  $4.35 \times 10^6 \text{ cm}^{-2} \text{ s}^{-1} \text{ sr}^{-1} \text{ MeV}^{-1}$  at  $E = 0.69$  MeV to  $1.16 \times 10^5 \text{ cm}^{-2} \text{ s}^{-1} \text{ sr}^{-1} \text{ MeV}^{-1}$  at  $E = 2.05$  MeV. The 1 in 100 year event (red line) exhibits a similar trend, lying in the range  $4.68 \times 10^6 \text{ cm}^{-2} \text{ s}^{-1} \text{ sr}^{-1} \text{ MeV}^{-1}$  to  $1.58 \times 10^5 \text{ cm}^{-2} \text{ s}^{-1} \text{ sr}^{-1} \text{ MeV}^{-1}$  and is a factor of 1.1 to 1.4 larger than the corresponding 1 in 10 year event. Figure 7d shows the shape parameter for the electron flux at  $L^* = 6.0$  as a function of energy. With the exception of the highest energy, the shape parameter is again negative suggesting that the relativistic electron fluxes at  $L^* = 6.0$  also have energy-dependent upper limits. The ratio of the 1 in 10 year flux at  $L^* = 4.5$  to that at  $L^* = 6.0$  increases with increasing energy ranging from 3.1 at  $E = 0.69$  MeV to 4.6 at  $E = 2.05$  MeV.

Finally, we repeated the analysis for each electron energy at the other  $L^*$  values. The 1 in 10, 1 in 50, and 1 in 100 year fluxes are summarized as a function of  $L^*$  for each energy in Figures 8a–8c, respectively. The 1 in 10 year flux of  $E = 0.69$  MeV electrons is roughly constant, of the order  $1.4 \times 10^7 \text{ cm}^{-2} \text{ s}^{-1} \text{ sr}^{-1} \text{ MeV}^{-1}$  in the range  $4.0 \leq L^* \leq 5.0$ , and then decreases with increasing  $L^*$  to  $1.6 \times 10^6 \text{ cm}^{-2} \text{ s}^{-1} \text{ sr}^{-1} \text{ MeV}^{-1}$  at  $L^* = 6.75$ . The 1 in 100 year flux of  $E = 0.69$  MeV electrons is generally a factor of 1.01 to 1.6 larger than the corresponding 1

Extreme Value Analysis of INTEGRAL IREM Electron Fluxes  
1 in N Year Electron Fluxes

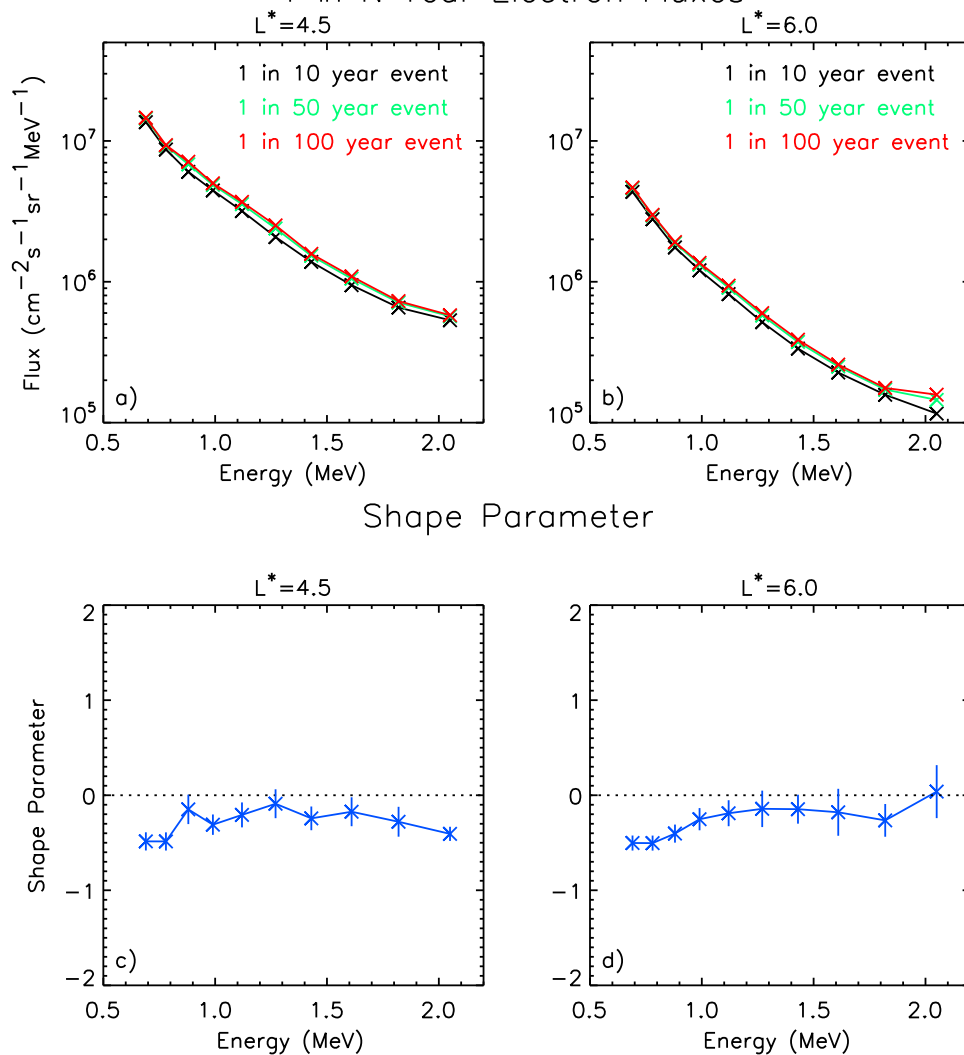


**Figure 7.** Plots of the 1 in *N* year flux as a function of energy for *N* = 10 (black), 50 (green), and 100 years (red) for (a) *L*\* = 4.5 and (b) *L*\* = 6.0 and the shape parameter as a function of energy for (c) *L*\* = 4.5 and (d) *L*\* = 6.0.

Extreme Value Analysis of INTEGRAL IREM Electron Fluxes  
1 in N Year Electron Fluxes versus *L*\*

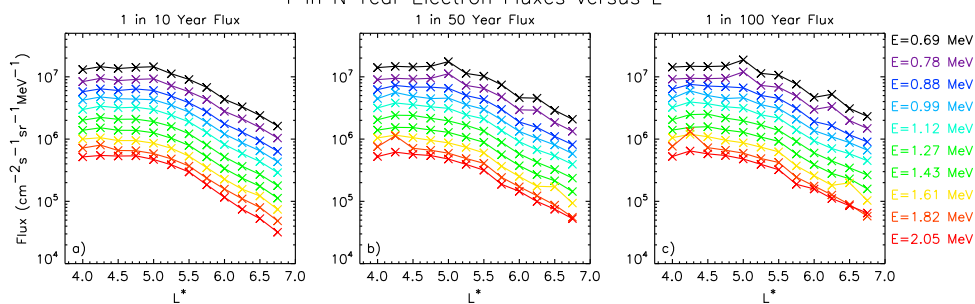


**Figure 8.** Plots of the 1 in *N* year flux as a function of *L*\* for each electron energy for (a) *N* = 10 years, (b) *N* = 50 years, and (c) *N* = 100 years.

in 10 year flux. At higher energies, the 1 in 10 year flux of  $E = 2.05$  MeV electrons is roughly constant, of the order  $5.3 \times 10^5 \text{ cm}^{-2} \text{ s}^{-1} \text{ sr}^{-1} \text{ MeV}^{-1}$  in the range  $4.0 \leq L^* \leq 4.75$  and then decreases with increasing  $L^*$  to  $3.2 \times 10^4 \text{ cm}^{-2} \text{ s}^{-1} \text{ sr}^{-1} \text{ MeV}^{-1}$  at  $L^* = 6.75$ . The 1 in 100 year flux of  $E = 2.05$  MeV electrons is a factor of 1.01 to 2.03 larger than the corresponding 1 in 10 year flux. The local maximum in the flux of the  $E = 1.82$  MeV flux at  $L^* = 4.25$  is not significant and due to a relatively poor fit at this energy and  $L^*$ .

## 6. Discussion

The extreme value analysis conducted here has determined the 1 in  $N$  year flux levels for relativistic electrons in the outer radiation belt ( $4.0 \leq L^* \leq 6.75$ ) in the energy range  $0.69 \leq E \leq 2.05$  MeV adding important information to our knowledge of extreme space weather events. Typically, more is known about extreme fluxes of energetic and relativistic electrons at geostationary orbit [O'Brien et al., 2007; Meredith et al., 2015] than at medium Earth orbit, in particular, near the magnetic equator. The results of this study show that the 1 in  $N$  year flux of relativistic electrons near the equator in medium Earth orbit are likely to be a factor of 3.1 to 4.6 times higher than that at geosynchronous orbit, depending on energy.

At geosynchronous orbit the difference between the 1 in 10 and 1 in 100 year flux of  $E = 2.05$  MeV electrons is a factor of 1.4. This is smaller than the difference of a factor of 4 found between the 1 in 10 and 1 in 100 year flux of  $E > 2$  MeV electrons at GOES West [Meredith et al., 2015]. The reason for this difference is possibly due to the fact the INTEGRAL IREM  $E = 2.05$  MeV flux is a differential flux, measured at a specific energy, whereas the GOES  $E > 2$  MeV flux is an integral flux and includes contributions from electrons at higher energies. During relativistic flux enhancements the tail of the electron distribution hardens [e.g., Meredith et al., 2002a], and consequently, there is an increased contribution from higher energies which will have a greater relative effect on the integral,  $E > 2$  MeV, fluxes. Thus, as the fluxes become more extreme, the  $E > 2$  MeV fluxes will increase more rapidly than the  $E = 2.05$  MeV fluxes. To investigate the difference further, it would be interesting to compare the results with similar analyses of data from the radiation monitor on XMM and the SREM instrument on Proba-1, which was launched a year earlier than INTEGRAL and had a more constant/regular coverage of the outer belt, albeit at low altitude.

The shape parameter in the region  $4.0 \leq L^* \leq 6.0$  is found to be predominantly negative suggesting that over this range of  $L^*$ , the relativistic electron flux tends toward a limiting value. Further out, conclusions cannot be drawn from the sign of the shape parameter since it is found to be predominantly close to zero with error bars which cross the zero level. The limiting value can be calculated for any given energy and  $L^*$  when the shape parameter is negative and is given by

$$x_L = u - \frac{\sigma}{\xi} \quad (5)$$

The limiting fluxes as a function of energy at  $L^* = 4.5$  and  $L^* = 6.0$  are tabulated in Table 5 and plotted in Figures 9a and 9b, respectively (blue traces). For comparison with the 1 in  $N$  year event levels the 1 in 10 and 1 in 100 year fluxes are included in the table and the 1 in 10 year fluxes are included in the plots (black traces). At  $L^* = 4.5$  the limiting fluxes lie in the range  $1.51 \times 10^7 \text{ cm}^{-2} \text{ s}^{-1} \text{ sr}^{-1} \text{ MeV}^{-1}$  at  $E = 0.69$  MeV to  $6.08 \times 10^5 \text{ cm}^{-2} \text{ s}^{-1} \text{ sr}^{-1} \text{ MeV}^{-1}$  at  $E = 2.05$  MeV and are up to factors of 2.3 and 1.9 times larger than the corresponding 1 in 10 and 1 in 100 year fluxes. Further out, at  $L^* = 6.0$  the limiting fluxes lie in the range  $4.82 \times 10^6 \text{ cm}^{-2} \text{ s}^{-1} \text{ sr}^{-1} \text{ MeV}^{-1}$  at  $E = 0.69$  MeV, to  $1.98 \times 10^5 \text{ cm}^{-2} \text{ s}^{-1} \text{ sr}^{-1} \text{ MeV}^{-1}$  at  $E = 1.82$  MeV and are up to factors of 1.5 and 1.4 times larger than the corresponding 1 in 10 and 1 in 100 year fluxes.

O'Brien et al. [2007] determined limiting fluxes of energetic electrons in geosynchronous orbit using data from the Los Alamos monitors from a 16 year period from 22 September 1989 to 24 September 2005. For relativistic electrons in the energy range 0.625–1.3 MeV, the flux limits derived from the Los Alamos monitors at geosynchronous orbit ranged from  $4.1 \times 10^6 \text{ cm}^{-2} \text{ s}^{-1} \text{ sr}^{-1} \text{ MeV}^{-1}$  at  $E = 0.625$  MeV, to  $10^6 \text{ cm}^{-2} \text{ s}^{-1} \text{ sr}^{-1} \text{ MeV}^{-1}$  at  $E = 1.30$  MeV. The limiting fluxes determined at 0.625, 0.9, and 1.3 MeV are plotted as red symbols in Figure 9b and are comparable in magnitude to the limiting fluxes derived from IREM (blue trace).

The presence of a limiting flux is consistent with the previous study of extreme fluxes from the Los Alamos monitors at geosynchronous orbit and two monitors in high Earth orbit [O'Brien et al., 2007]. This contrasts with the results of a recent extreme value analysis of relativistic electron fluxes at geosynchronous orbit, using GOES data from January 1995 to June 2014, which found evidence to suggest that the daily average flux of  $E > 2$  MeV electrons does not tend to a limiting value [Meredith et al., 2015]. However, when the analysis

**Table 5.** One in 10 year, 1 in 100 year, and Limiting Fluxes at  $L^* = 4.5$  and  $L^* = 6.0$

Energy (MeV)	$L^* = 4.5$			$L^* = 6.0$		
	1 in 10 year Flux ( $\text{cm}^2 \text{ s sr MeV}^{-1}$ )	1 in 100 year Flux ( $\text{cm}^2 \text{ s sr MeV}^{-1}$ )	Limiting Flux ( $\text{cm}^2 \text{ s sr MeV}^{-1}$ )	1 in 10 year Flux ( $\text{cm}^2 \text{ s sr MeV}^{-1}$ )	1 in 100 year Flux ( $\text{cm}^2 \text{ s sr MeV}^{-1}$ )	Limiting Flux ( $\text{cm}^2 \text{ s sr MeV}^{-1}$ )
0.69	$1.36 \times 10^7$	$1.46 \times 10^7$	$1.51 \times 10^7$	$4.35 \times 10^6$	$4.68 \times 10^6$	$4.82 \times 10^6$
0.78	$8.69 \times 10^6$	$9.34 \times 10^6$	$9.66 \times 10^6$	$2.78 \times 10^6$	$2.99 \times 10^6$	$3.09 \times 10^6$
0.88	$6.03 \times 10^6$	$7.11 \times 10^6$	$9.78 \times 10^6$	$1.75 \times 10^6$	$1.91 \times 10^6$	$2.02 \times 10^6$
0.99	$4.45 \times 10^6$	$5.00 \times 10^6$	$5.53 \times 10^6$	$1.21 \times 10^6$	$1.36 \times 10^6$	$1.56 \times 10^6$
1.12	$3.18 \times 10^6$	$3.69 \times 10^6$	$4.56 \times 10^6$	$8.18 \times 10^5$	$9.39 \times 10^5$	$1.16 \times 10^6$
1.27	$2.08 \times 10^6$	$2.52 \times 10^6$	$4.74 \times 10^6$	$5.17 \times 10^5$	$5.99 \times 10^5$	$8.11 \times 10^5$
1.43	$1.38 \times 10^6$	$1.58 \times 10^6$	$1.83 \times 10^6$	$3.36 \times 10^5$	$3.88 \times 10^5$	$5.19 \times 10^5$
1.61	$9.47 \times 10^5$	$1.09 \times 10^6$	$1.38 \times 10^6$	$2.27 \times 10^5$	$2.59 \times 10^5$	$3.20 \times 10^5$
1.82	$6.56 \times 10^5$	$7.29 \times 10^5$	$8.10 \times 10^5$	$1.58 \times 10^5$	$1.76 \times 10^5$	$1.98 \times 10^5$
2.05	$5.34 \times 10^5$	$5.79 \times 10^5$	$6.08 \times 10^5$	$1.16 \times 10^5$	$1.58 \times 10^5$	-

was repeated using the log of the daily average fluxes for comparison with *O'Brien et al.* [2007], the results were not conclusive, suggesting that the result be treated with some caution. The results of a similar extreme value analysis of internal charging currents in medium Earth orbit, using Giove-A SURF data from December 2005 to January 2016, suggested that the daily average internal charging currents due to electrons with energies greater than 1.1 MeV does not tend to an upper limit [*Meredith et al.*, 2016a], but the results for internal charging currents due to lower energy electrons ( $E > 700$  and  $E > 900$  keV) were not conclusive due to the size of the error bars on the shape parameter. This contrasts with results from low Earth orbit, based on POES data between July 1998 and June 2014, which suggested that the  $E > 100$  keV electrons and  $E > 300$  keV electrons do not have an upper bound [*Meredith et al.*, 2016b]. The current study examined differential fluxes whereas the three recent studies of *Meredith et al.* [2015, 2016a, 2016b] examined either integral fluxes or charging currents caused by electrons with a wide range of incident energies. One possible explanation for the differing results is that the hardening spectra associated with more extreme events could give rise to different behavior in the tail of the distribution for integral and differential fluxes. Other possibilities include differences in time periods used for the analyses and the inherent difficulty of using 10 to 20 years data to infer the presence or absence of an upper limit which may typically not be reached for 100 years or more. This suggests

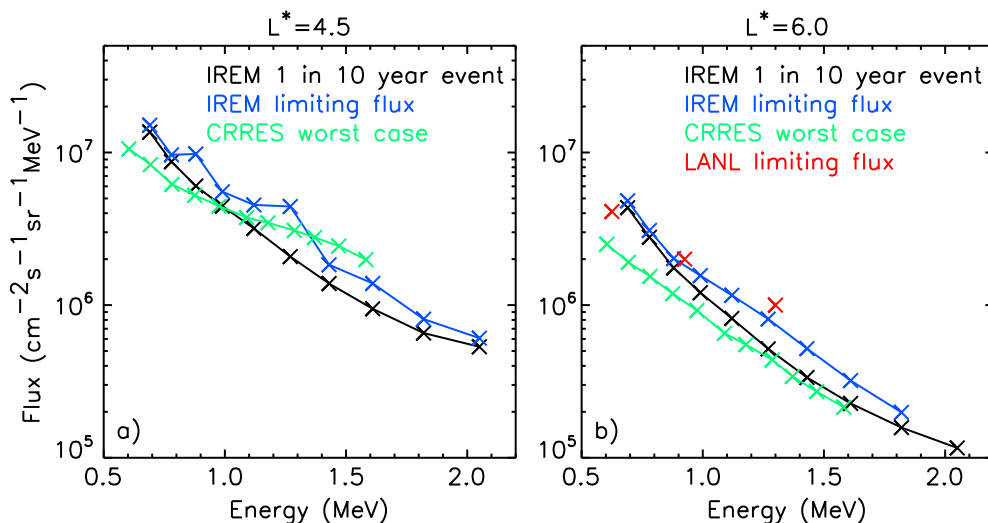


**Figure 9.** Plot of the IREM limiting flux (blue trace) as a function of energy at (a)  $L^* = 4.5$  and (b)  $L^* = 6.0$ . The corresponding 1 in 10 year flux determined from IREM (black trace) and the CRRES worst case fluxes (green trace) are shown for comparison in each plot. The LANL limiting fluxes (red symbols) at geosynchronous orbit are shown for comparison in Figure 9b.

that more data, over a considerably extended time period, is likely to be required to fully resolve this issue. In reality a physical process or set of processes is likely to ultimately establish an upper bound, consistent with the current findings.

The Medium Electrons A instrument on board the Combined Release and Radiation Effects Satellite (CRRES) measured electrons in the energy range 0.153 MeV to 1.58 MeV [Vampola *et al.*, 1992], covering a significant fraction of the energy range analyzed here. The CRRES mission lasted for only 15 months and is not suited to an extreme value analysis to determine the 1 in 10 and 1 in 100 year fluxes. However, the largest daily average flux of  $E > 2$  MeV electrons observed by GOES at geosynchronous orbit in the 13.67 year period from 1 January 1986 to 31 August 1999, of  $7.94 \times 10^4 \text{ cm}^{-2} \text{ s}^{-1} \text{ sr}^{-1}$ , occurred on 28 March 1991 during the CRRES mission [Fennell *et al.*, 2000; Koons, 2001]. Based on these data, the experimental return period of this event is thus 13.67 years and we might expect the fluxes observed to be similar in magnitude to a 1 in 10 year event. It is thus instructive to compare the 1 in 10 year fluxes reported here with the largest fluxes observed during the CRRES mission. We rebinned the CRRES MEA data as a function of  $L^*$  and half orbit, using similar techniques to those adopted in Meredith *et al.* [2002b] and determined the maximum flux as a function of energy at  $L^* = 4.5$  and 6.0 for comparison with the IREM results. The largest fluxes of relativistic electrons observed during the CRRES mission at  $L^* = 6.0$  in the energy range 0.62–1.58 MeV occurred on 28/29 March 1991 and are plotted in Figure 9b (green trace). The fluxes are similar in magnitude to the 1 in 10 year flux observed by IREM and about a factor of 2 less than the limiting fluxes. The largest fluxes of relativistic electrons observed during the CRRES mission at  $L^* = 4.5$ , which also occurred on 28/29 March 1991, are plotted in Figure 9a (green trace). The fluxes are also similar in magnitude to the 1 in 10 year fluxes observed by IREM, although the former show evidence of a harder spectrum. The overall agreement with the CRRES and LANL data is very good and give us confidence in the IREM results presented here.

The worst case daily average flux of GOES  $E > 2$  MeV electrons, observed in the period between 1 January 1986 and 31 August 1999 on 28 March 1991, was used, together with data from CRRES and LANL at  $L \sim 6.6$  on the same date, to construct a worst case average spectrum for geosynchronous orbit [Fennell *et al.*, 2000]. A question raised in the paper was how often are the extreme levels in the worst case spectrum realized? Using recent observations from the GOES spacecraft, we find that in the 19.5 year period between 1 January 1995 and 30 June 2014, the daily average  $E > 2$  MeV flux exceeded  $7.94 \times 10^4 \text{ cm}^{-2} \text{ s}^{-1} \text{ sr}^{-1}$  14 times at GOES West, associated with six independent relativistic enhancement events. Furthermore, the largest observed daily average flux of  $E > 2$  MeV electrons at GOES West during this period, of  $4.92 \times 10^5 \text{ cm}^{-2} \text{ s}^{-1} \text{ sr}^{-1}$  on 29 July 2004, exceeded the value on 28 March 1991 by a factor of 6.2 [Meredith *et al.*, 2015].

Inspection of the geomagnetic and solar wind conditions for the top 10 events at  $L^* = 4.5$  and 6.0 shows that these events are associated with geomagnetically disturbed periods driven by both coronal mass ejections (CMEs) and high-speed solar wind streams. CME-driven storms are sporadic in nature, can occur during any phase of the solar cycle, and peak at solar maximum [St. Cyr *et al.*, 2000]. In contrast, storms driven by high-speed solar wind streams maximize in the declining phase [Burlaga and Lepping, 1977; Gonzalez *et al.*, 1999] and tend to recur with a periodicity of 27 days due to the solar rotation. Since accumulated charge takes time to decay [e.g., Bodeau, 2010], recurrent enhanced fluxes of relativistic electrons driven by high-speed solar wind streams in the declining phase could be a particular threat to the satellite fleet. There is important evidence for this in the increase in the number of satellite anomalies attributed to IESD during the last 118 days of 2016 (Figure 2). For example, based on information from 37 satellites in geosynchronous orbit, only four anomalies were attributed to IESD during the relatively quiet 83 day period between 15 May and 6 August (D. Pitchford, personal communication, 2017). During this interval, the fluxes of  $E = 2.05$  MeV and  $E > 2$  MeV electrons were typically less than  $2 \times 10^4 \text{ cm}^{-2} \text{ s}^{-1} \text{ sr}^{-1} \text{ MeV}^{-1}$  and  $10^4 \text{ cm}^{-2} \text{ s}^{-1} \text{ sr}^{-1}$ , respectively. In sharp contrast, 41 anomalies were attributed to IESD during the last 118 days of the year (D. Pitchford, personal communication, 2017). During this period there were eight high-speed solar wind streams with peak velocities above  $700 \text{ km s}^{-1}$ , and peak fluxes of  $E = 2.05$  MeV electrons, as measured by IREM at  $L^* = 6.0$ , typically greater than  $5 \times 10^4 \text{ cm}^{-2} \text{ s}^{-1} \text{ sr}^{-1} \text{ MeV}^{-1}$  and peak fluxes of  $E > 2$  MeV electrons, as measured by GOES, typically greater than  $5 \times 10^4 \text{ cm}^{-2} \text{ s}^{-1} \text{ sr}^{-1}$ .

It is instructive to compare the results of this analysis with current models of worst case relativistic electrons in the outer radiation belt. At  $L^* = 6.0$ , representative of geosynchronous orbit, the 1 in 10 year fluxes in the range  $E = 1$  to 2 MeV are about 2 times higher than the 99th percentile of the *AE9 static model* and about 1.6 to 2.8 times higher than the 99th percentile of the Model of Outer Belt Electrons for Dielectric Internal

Charging (MOBE-DIC) model [Hands et al., 2015]. We note that the percentiles for AE9 and MOBE-DIC are not the same — representing confidence limits and exceedance probabilities, respectively. Further in, at  $L^* = 4.5$ , representative of the peak fluxes encountered in GNSS type environments, the 1 in 10 year fluxes are about 1.4 to 1.5 times higher than the 99th percentile of the AE9 static model and about 1.01 to 2 times higher than the 99th percentile of the MOBE-DIC model [Hands et al., 2015].

## 7. Conclusions

We have conducted an extreme value analysis of the electron flux in the outer radiation belt near the magnetic equator as a function of energy and  $L^*$  using data from the IREM instrument on the INTEGRAL satellite. Our principal results are as follows:

1. The 1 in 10 year flux at  $L^* = 4.5$ , in the vicinity of equatorial medium Earth orbit, decreases with increasing energy ranging from  $1.36 \times 10^7 \text{ cm}^{-2} \text{ s}^{-1} \text{ sr}^{-1} \text{ MeV}^{-1}$  at  $E = 0.69 \text{ MeV}$  to  $5.34 \times 10^5 \text{ cm}^{-2} \text{ s}^{-1} \text{ sr}^{-1} \text{ MeV}^{-1}$  at  $E = 2.05 \text{ MeV}$ . The 1 in 100 year flux at  $L^* = 4.5$  is a factor of 1.1 to 1.2 larger than the corresponding 1 in 10 year flux.
2. The 1 in 10 year flux at  $L^* = 6.0$ , in the vicinity of geosynchronous orbit, decreases with increasing energy ranging from  $4.35 \times 10^6 \text{ cm}^{-2} \text{ s}^{-1} \text{ sr}^{-1} \text{ MeV}^{-1}$  at  $E = 0.69 \text{ MeV}$  to  $1.16 \times 10^5 \text{ cm}^{-2} \text{ s}^{-1} \text{ sr}^{-1} \text{ MeV}^{-1}$  at  $E = 2.05 \text{ MeV}$ . The 1 in 100 year flux at  $L^* = 6.0$  is a factor of 1.1 to 1.4 larger than the corresponding 1 in 10 year flux.
3. The 1 in 10 year flux of  $E = 0.69 \text{ MeV}$  electrons is roughly constant, of the order  $1.4 \times 10^7 \text{ cm}^{-2} \text{ s}^{-1} \text{ sr}^{-1} \text{ MeV}^{-1}$  in the range  $4.0 \leq L^* \leq 5.0$  and then decreases with increasing  $L^*$  to  $1.6 \times 10^6 \text{ cm}^{-2} \text{ s}^{-1} \text{ sr}^{-1} \text{ MeV}^{-1}$  at  $L^* = 6.75$ . The 1 in 100 year flux of  $E = 0.69 \text{ MeV}$  electrons is generally a factor of 1.01 to 1.6 larger than the corresponding 1 in 10 year flux.
4. The 1 in 10 year flux of  $E = 2.05 \text{ MeV}$  electrons is roughly constant, of the order  $5.3 \times 10^5 \text{ cm}^{-2} \text{ s}^{-1} \text{ sr}^{-1} \text{ MeV}^{-1}$  in the range  $4.0 \leq L^* \leq 4.75$  and then decreases with increasing  $L^*$  to  $3.2 \times 10^4 \text{ cm}^{-2} \text{ s}^{-1} \text{ sr}^{-1} \text{ MeV}^{-1}$  at  $L^* = 6.75$ . The 1 in 100 year flux of  $E = 2.05 \text{ MeV}$  electrons is a factor of 1.01 to 2.03 larger than the corresponding 1 in 10 year flux.
5. The ratio of the 1 in 10 year flux at  $L^* = 4.5$  to that at  $L^* = 6.0$  increases with increasing energy ranging from 3.1 at  $E = 0.69 \text{ MeV}$  to 4.6 at  $E = 2.05 \text{ MeV}$ .

The 1 in  $N$  year electron fluxes determined here as a function of energy and  $L^*$  can serve as benchmarks against which to compare other extreme space weather events and to help assess the potential impact of an extreme event.

## References

- Baker, D. N., J. B. Blake, L. B. Callis, J. R. Cummings, D. Hovestadt, S. Kanekal, B. Klecker, R. A. Mewaldt, and R. D. Zwickl (1994), Relativistic electron acceleration and decay time scales in the inner and outer radiation belts: SAMPEX, *Geophys. Res. Lett.*, *21*, 409–412.
- Blake, J. B., W. A. Kolasinski, R. W. Fillius, and E. G. Mullen (1992), Injection of electrons and protons with energies of tens of MeV into  $L < 3$  on 24 March 1991, *Geophys. Res. Lett.*, *19*(8), 821–824.
- Blake, J. B., et al. (2013), The Magnetic Electron Ion Spectrometer (MagEIS) Instruments Aboard the Radiation Belt Storm Probes (RBSP) Spacecraft, *Space Sci. Rev.*, *179*, 383, doi:10.1007/s11214-013-9991-8.
- Bodeau, M. (2010), High energy electron climatology that supports deep charging risk assessment in GEO, in *48th AIAA Aerospace Sciences Meeting Including the New Horizons Forum and Aerospace Exposition, Aerospace Sciences Meetings*, AIAA, Orlando, Fla., doi:10.2514/6.2010-1608.
- Burlaga, L. F., and R. P. Lepping (1977), The causes of recurrent geomagnetic storms, *Planet. Space Sci.*, *25*, 1151–1160.
- Cabinet Office (2012), National Risk Register of Civil Emergencies, 70 Whitehall, London, SW1A 2AS. [Available at <http://www.cabinetoffice.gov.uk/>]
- Coles, S. (2001), *An Introduction to Statistical Modelling of Extreme Values*, Springer, London.
- Evans, H. D. R., P. Bühler, W. Hajdas, E. J. Daly, P. Nieminen, and A. Mohammadzadeh (2008), Results from the ESA SREM monitors and comparison with existing radiation belt models, *Adv. Space Res.*, *42*, 1527–1537.
- Fennell, J. F., H. C. Koons, M. W. Chen, and J. B. Blake (2000), Internal charging: A preliminary environmental specification for satellites, *IEEE Trans. Plasma Sci.*, *28*, 2029–2036, doi:10.1109/27.902230.
- Frederickson, A. R., E. G. Mullen, D. H. Brautigam, K. J. Kerns, and E. G. Holman (1991), Radiation induced insulator discharge pulses in the CRRES internal discharge monitor satellite experiment, *IEEE Trans. Nucl. Sci.*, *38*, 778–784.
- Gonzalez, W. D., B. T. Tsurutani, and A. L. Clua de Gonzalez (1999), Interplanetary origin of geomagnetic storms, *Space Sci. Rev.*, *88*, 529–562.
- Hands, A. D. P., K. A. Ryden, C. Underwood, D. Rodgers, and H. D. R. Evans (2015), A new model of outer belt electrons for dielectric internal charging (MOBE-DIC), *IEEE Trans. Nucl. Sci.*, *62*, 2767–2775.
- Heffernan, J. E., A. G. Stephenson, and E. Gilleland (2014), ISMEV: An introduction to statistical modeling of extreme values, version 1.39. [Available at <http://www.ral.ucar.edu/ericg/softextreme.php>]
- Höcker, A., and V. Kartvelishvili (1996), SVD approach to data unfolding, *Nuclear Instrum. Methods Phys. Res.*, *372*, 469–481.
- Horne, R. B., and D. Pitchford (2015), Space weather concerns for all-electric propulsion satellites, *Space Weather*, *13*, 430–433, doi:10.1002/2015SW001198.

### Acknowledgments

We would like to thank David Pitchford, Justin Likar, and David Wade for useful discussions. We also thank NASA/GSFC's Space Physics Data Facility's OMNIWeb service for provision of the solar wind and geophysical parameters used in this study. The research leading to these results has received funding from the European Union Seventh Framework Programme (FP7/2007-2013) under grant agreement 606716 (SPACESTORM) and the Natural Environment Research Council. Part of this work has been supported by ESA/ESTEC contract 4000111777/14/NL/HK. The UNILIB library used in this study was developed by the Belgian Institute for Space Aeronomy under ESA/GSTP funding and is available at <http://www.mag-unilib.eu/>. For the cross calibrations we used the MAGEIS data (Release 03, Level 2, Version 4.X) from RBSP-B available from [https://rbsp-ect.lanl.gov/data\\_pub/rbspb/mageis/level2/sectors/](https://rbsp-ect.lanl.gov/data_pub/rbspb/mageis/level2/sectors/). The GOES data used in the production of Figure 2 are available from [https://satdat.ngdc.noaa.gov/sem/goes/data/new\\_avg](https://satdat.ngdc.noaa.gov/sem/goes/data/new_avg). The CRRES MEA data used in this study were provided by Al Vampola and Daniel Heynderickx and are available on request. The IREM proton and electron fluxes, unfolded (as Level 1) and cross-calibrated (as Level 2) will become available from <http://srem.web.psi.ch> within the next couple of months. The data used to generate the plots in this paper are available on request.

- Horne, R. B., N. P. Meredith, R. M. Thorne, D. Heynderickx, R. H. A. Iles, and R. R. Anderson (2003), Evolution of energetic electron pitch angle distributions during storm time electron acceleration to megaelectronvolt energies, *J. Geophys. Res.*, *108*(A1), 1016, doi:10.1029/2001JA009165.
- Hübner, J. M., et al. (2012), *INTEGRAL revisits Earth—Perigee Effects on Spacecraft Components*, paper presented at AIAA SpaceOps Conference, Am. Inst. of Aeronaut. and Astronaut., Stockholm, Sweden, 11–15 June.
- Iucci, N., et al. (2005), Space weather conditions and spacecraft anomalies in different orbits, *Space Weather*, *3*, S01001, doi:10.1029/2003SW000056.
- Koons, H. C., and J. F. Fennell (2006), Space weather effects on communications satellites, *Sci. Bull. Int. Union Radio Sci.*, *316*, 27–41.
- Koons, H. C. (2001), Statistical analysis of extreme values in space science, *J. Geophys. Res.*, *106*(A6), 10,915–10,921, doi:10.1029/2000JA000234.
- Krausmann, E. (2011), The space-weather awareness dialogue: Findings and outlook, *JRC Sci. Tech. Rep.*, Publ. Off. of the Eur. Union, Luxembourg.
- Meredith, N. P., R. B. Horne, D. Summers, R. M. Thorne, R. H. A. Iles, D. Heynderickx, and R. R. Anderson (2002a), Evidence for acceleration of outer zone electrons to relativistic energies by whistler mode chorus, *Ann. Geophys.*, *20*, 967–979.
- Meredith, N. P., R. B. Horne, R. H. A. Iles, R. M. Thorne, R. R. Anderson, and D. Heynderickx (2002b), Outer zone relativistic electron acceleration associated with substorm-enhanced whistler mode chorus, *J. Geophys. Res.*, *107*(A7), 1144, doi:10.1029/2001JA900146.
- Meredith, N. P., R. B. Horne, J. D. Isles, and J. V. Rodriguez (2015), Extreme relativistic electron fluxes at geosynchronous orbit: Analysis of GOES  $E > 2$  MeV electrons, *Space Weather*, *13*, 170–184, doi:10.1002/2014SW001143.
- Meredith, N. P., R. B. Horne, J. D. Isles, K. A. Ryden, A. D. P. Hands, and D. Heynderickx (2016a), Extreme internal charging currents in medium Earth orbit: Analysis of SURF plate currents on Giove-A, *Space Weather*, *14*, 578–591, doi:10.1002/2016SW001404.
- Meredith, N. P., R. B. Horne, J. D. Isles, and J. C. Green (2016b), Extreme energetic electron fluxes in low Earth orbit: Analysis of POES  $E > 30$ ,  $E > 100$  and  $E > 300$  keV electrons, *Space Weather*, *14*, 136–150, doi:10.1002/2015SW001348.
- Mohammadzadeh, A., et al. (2003), The ESA standard radiation environment monitor program first results from Proba-I and INTEGRAL, *IEEE Trans. Nucl. Sci.*, *50*, 2272–2277.
- National Science and Technology Council (2015), National Space Weather Action Plan, Space Weather Oper., Res. and Mitigation Subcomm., Executive Off. of the President of the U.S., Washington, D. C. [Available at [https://www.whitehouse.gov/sites/default/files/microsites/ostp/final\\_national\\_space\\_weather\\_action\\_plan\\_20151028.pdf](https://www.whitehouse.gov/sites/default/files/microsites/ostp/final_national_space_weather_action_plan_20151028.pdf).]
- O'Brien, T. P., J. F. Fennell, J. L. Roeder, and G. D. Reeves (2007), Extreme electron fluxes in the outer zone, *Space Weather*, *5*, S01001, doi:10.1029/2006SW000240.
- Olson, W. P., and K. Pfizter (1977), *Magnetospheric Magnetic Field Modelling Annual Scientific Report*, Air Force Off. of Sci. Res., Arlington, Va.
- Onsager, T. G., R. Grubb, J. Kunches, L. Matheson, D. Speich, R. Zwickl, and H. Sauer (1996), Operational uses of the GOES energetic particle detectors, in GOES-8 and beyond, *Proc. SPIE Int. Soc. Opt. Eng.*, *2812*, 281–290.
- Picklands, J. (1975), Statistical inference using extreme order statistics, *Ann. Stat.*, *3*, 119–131.
- R Development Core Team (2008), *R: A Language and Environment for Statistical Computing*, R Foundation for Statistical Computing, Vienna, Austria. [Available at <http://www.R-project.org/>.]
- Rodgers, D. J., and K. A. Ryden (2001), Internal charging in space, in *Spacecraft Charging Technology, Proceedings of the Seventh International Conference held 23–27 April, 2001 at ESTEC*, edited by R. A. Harris, p.25, European Space Agency, ESA SP-476, Noordwijk, Netherlands.
- St. Cyr, O., et al. (2000), Properties of coronal mass ejections: SOHO LASCO observations from January 1996 to June 1998, *J. Geophys. Res.*, *105*, 18,169–18,185.
- Sandberg, I., et al. (2012), Unfolding and validation of SREM fluxes, *IEEE Trans. Nucl. Sci.*, *59*, 1105–1112.
- Sandberg, I., et al. (2014), Cross-calibration of NOAA GOES solar proton detectors using corrected NASA IMP-8/GME data, *Geophys. Res. Lett.*, *41*, 4435–4441, doi:10.1002/2014GL060469.
- Satellite Industry Association (2016), State of the satellite industry report 2016, The Tauri Group, Alexandria, Va. [Available at <http://www.sia.org/state-of-the-satellite-industry-report/2014-sia-state-of-satellite-industry-report/>.]
- Siegl, M., H. D. R. Evans, E. J. Daly, G. Santin, P. J. Nieminen, and P. Buhler (2010), Inner belt anisotropy investigations based on the Standard Radiation Environment Monitor (SREM), *IEEE Trans. Nucl. Sci.*, *57*, 2017–2023, doi:10.1109/TNS.2010.2041253.
- Strategic National Risk Assessment (2011), Department of Homeland Security, Washington, D. C. [Available at <http://www.dhs.gov/strategic-national-risk-assessment-snra>.]
- Vampola, A. L., J. V. Osborn, and B. M. Johnson (1992), CRRES magnetic electron spectrometer, *J. Spacecr. Rockets*, *29*, 592–595.
- Webb, F. D., and J. H. Allen (2004), Spacecraft and ground anomalies related to the October–November 2003 solar activity, *Space Weather*, *2*, S03008, doi:10.1029/2004SW000075.
- Wrenn, G. L. (1995), Conclusive evidence for internal dielectric charging anomalies on geosynchronous communications spacecraft, *J. Spacecr. Rockets*, *32*, 514–520.
- Wrenn, G. L., D. J. Rodgers, and K. A. Ryden (2002), A solar cycle of spacecraft anomalies due to internal charging, *Ann. Geophys.*, *20*, 953–956.